Hindawi
Modelling and Simulation in Engineering
Volume 2022, Article ID 3698887, 19 pages
https://doi.org/10.1155/2022/3698887

Research Article

Effects of Baffle Height and Baffle Location on Heat Transfer and Flow Profiles in a Baffled Duct: A CFD Analysis

Amnart Boonloi[1] **and Withada Jedsadaratanachai**[2]

[1]*Department of Mechanical Engineering Technology, College of Industrial Technology, King Mongkut's University of Technology North Bangkok, Bangkok 10800, Thailand*
[2]*Department of Mechanical Engineering, School of Engineering, King Mongkut's Institute of Technology Ladkrabang, Bangkok 10520, Thailand*

Correspondence should be addressed to Withada Jedsadaratanachai; withada.je@kmitl.ac.th

Received 24 March 2022; Revised 2 June 2022; Accepted 15 June 2022; Published 1 July 2022

Academic Editor: Houari Ameur

CFD analysis of flow and heat transfer characteristics in a baffled duct is reported. The baffle locations ($s = 0.05H - 0.40H$), flow paths (V-apex directing Downstream or VD and V-apex directing Upstream or VU), and baffle heights ($b = 0.05H - 0.30H$) are investigated in the laminar flow regime with the Reynolds number based on the entry conditions between 100 and 2,000. Solutions of the present work are obtained by the finite volume method (a commercial code). Key mechanisms such as fluid streams, impinging streams, and disturbed thermal boundary layer in the baffled duct are observed. The baffle locations have high impact on flow and heat transfer behavior. The best heat transfer rate of the baffled duct is 15.55 times higher than that of the general duct with no baffle, while the optimum TEF is 4.06.

1. Introduction

V-pattern rib/baffle is a kind of vortex generators frequently used to change thermal behavior and flow profiles in heat exchangers. The changes of flow and thermal profiles improve heat transfer coefficient and thermal efficiency. The V-pattern rib/baffle is more effective in improving efficiency of heat exchangers compared with other types of vortex generators [1]. The V-pattern rib/baffle has been developed with two main aims: (1) to improve the heat transfer in the heat exchangers and (2) to facilitate installation, manufacturing, and maintenance. Moreover, it is recommended that the structural rib/baffle must be stable for the installation in the heat exchangers.

Researchers have investigated thermal development in different types of heat exchangers with V-pattern rib/baffles (or similarity shape). Zhang et al. [2] studied the forced convective heat transfer in a channel installed with micro V-pattern ribs and dimples at the Re number of 50,500. They found that the combined vortex generator (micro V-pattern rib-dimple hybrid configuration) resulted in the higher heat transfer coefficient compared with the generator with only V-pattern ribs or dimples. Xiao et al. [3] studied the enhanced heat transfer efficiency of a mini-channel heat sink with V-pattern ribs. They stated that the Nusselt number of their study was 1.71–3.55 times higher than the base case. Bahiraei et al. [4] selected V-pattern ribs combined with nanofluid to improve the second law characteristics of fluid flow behavior in a square channel. Jain and Lanjewar [5] presented the overview of V-pattern rib geometries in a solar air heater and performance analysis. The effects of relative roughness pitches with single relative staggered rib were considered. They concluded that the maximum Nu/Nu_0 and f/f_0 of the solar air heater are around 2.30 and 3.18, respectively. Jin et al. [6] numerically simulated the augmented thermal efficiency in a solar air heater roughened by multiple V-pattern ribs. They found that the optimum number of spanwise ribs declined with an increase in the channel height, the angle of attack, and relative rib spacing. Bahiraei et al. [7] simulated the thermal performance of

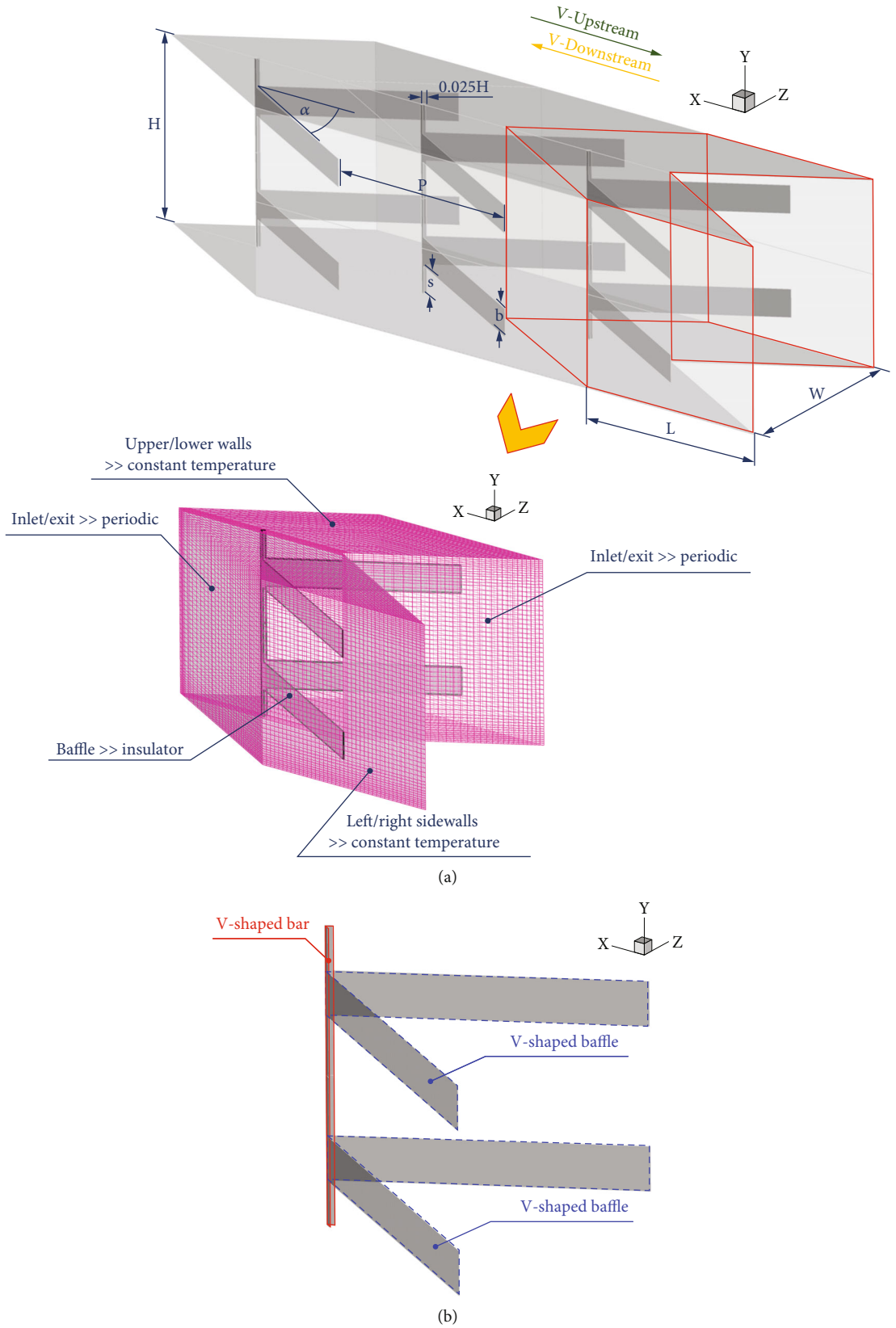

Figure 1: Physical domain of (a) baffled duct and (b) baffle configuration.

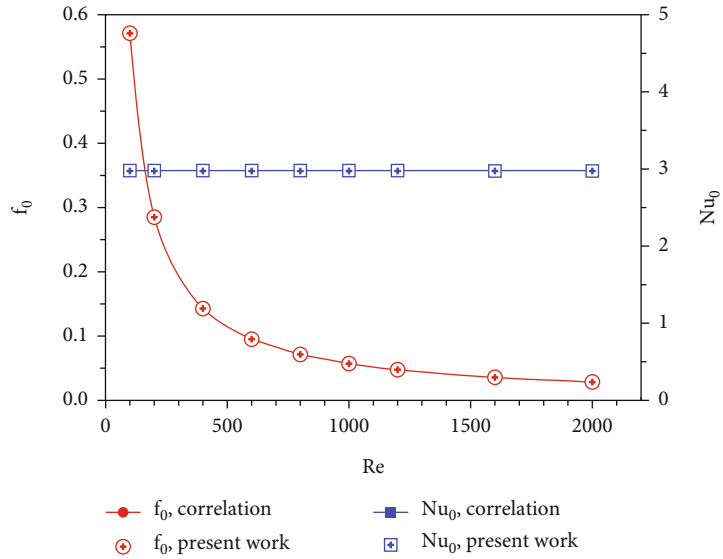

Figure 2: Validation of smooth square duct.

Cu-water nanofluid within a square channel installed with 90° V-shaped ribs. The numerical analysis of fluid flow and heat transfer profiles in a solar air heater using V-down ribs with multiple gaps were performed by Misra et al. [8]. Jin et al. [9] reported the best thermal performance for a solar air heater inserted with staggered multiple V-pattern ribs as 2.43. Jin et al. [10] numerically studied the influences of multiple V-pattern ribs on the absorber plate in a solar air heater. The best thermal performance reported is 1.93. Kumar and Kim [11] found that the combined vortex generator (V-pattern rib and groove roughness) performs better in terms of thermal efficiency compared with other V-pattern rib roughness shapes. The effects of V-down ribs with gaps at various flow attack angles (30°–75°) in a rectangular duct were examined by Singh et al. [12]. Their best flow attack angle is 60°. Deo et al. [13] experimentally analyzed the performance of a duct roughened with multigap V-down ribs combined with staggered ribs. The rib pitch-to-height ratios, rib height-to-hydraulic diameter ratios, and angles of attack were considered in their study. They reported the enhanced heat transfer of 3.34 times higher than that of the base case. Ravi and Saini [14] studied the forced convection in a solar heater with discrete multi-V-shaped and staggered rib roughness on both sides of the absorber plate. Caliskan and Baskaya [15] experimentally investigated the impinging jet array heat transfer from a surface with V-pattern and convergent-divergent ribs. Singh et al. [16] presented the exergy analysis of a solar air heater using discrete V-down rib on the absorber plate. Karwa and Chitoshiya [17] experimentally studied the selection of discrete V-down ribs to augment the heat transfer rate in a solar heater. Their results indicated the enhanced thermal efficiency of 12.5–20%. The experimental investigations of heat transfer in a two-pass channel using V-pattern ribs and cylindrical dimples were presented by Singh and Ekkad [18]. Kumar et al. [19] reported the Nusselt number and friction factor correlations of a solar air heater having with multi-V-pattern ribs with gaps. They found their highest Nusselt number to be 6.74 times higher than the base case. The experimental results on the thermal performance improvement of a double pass duct with roughness elements (discrete multi-V-pattern and staggered ribs) were reported by Ravi and Saini [20]. Boruah et al. [21, 22] reported the entropy analysis for mixed convective flows over a backward facing step channel with baffle. They found that the elliptical baffle is an optimum design for staggered arrangement.

From the literature review and our related works [1], we found that the location of the V-shaped rib/baffle has high impact on the variations of fluid flow and heat transfer patterns. Thus, in the present work, we include these factors into consideration for the V-shaped rib/baffle modification. First, the V-shaped rib/baffle is modified with the objective to increase structural stabilization. Second, the location in a cross-sectional plane in the tested duct is considered. The numerical method is employed to examine flow and heat transfer characteristics. The flow pattern and heat transfer profiles are important data for the heat transfer improvement. The knowledge of the fluid flow and heat transfer mechanisms in the tested duct is the key to improvement of heat exchanger efficiency.

2. Baffled Duct, Computational Domain, and Boundary Conditions

The baffled duct and computational domain with boundary conditions are illustrated in Figure 1(a), while the modified V-shaped baffle is presented in Figure 1(b). Hydraulic diameter, D_h, of the baffled duct is equivalent to 0.05 m ($H = W = D_h = 0.05$ m). The baffles are inserted in the duct with a pitch distance, $P = 0.05$ m or $P = H$. The angle of attack or inclination angle of the baffle is fixed at 30° for all investigated cases. The baffle height, b, is varied: $b =$ 0.05H, 0.10H, 0.15H, 0.20H, 0.25H, and 0.30H. The distance between the upper-lower duct walls and the upper-lower

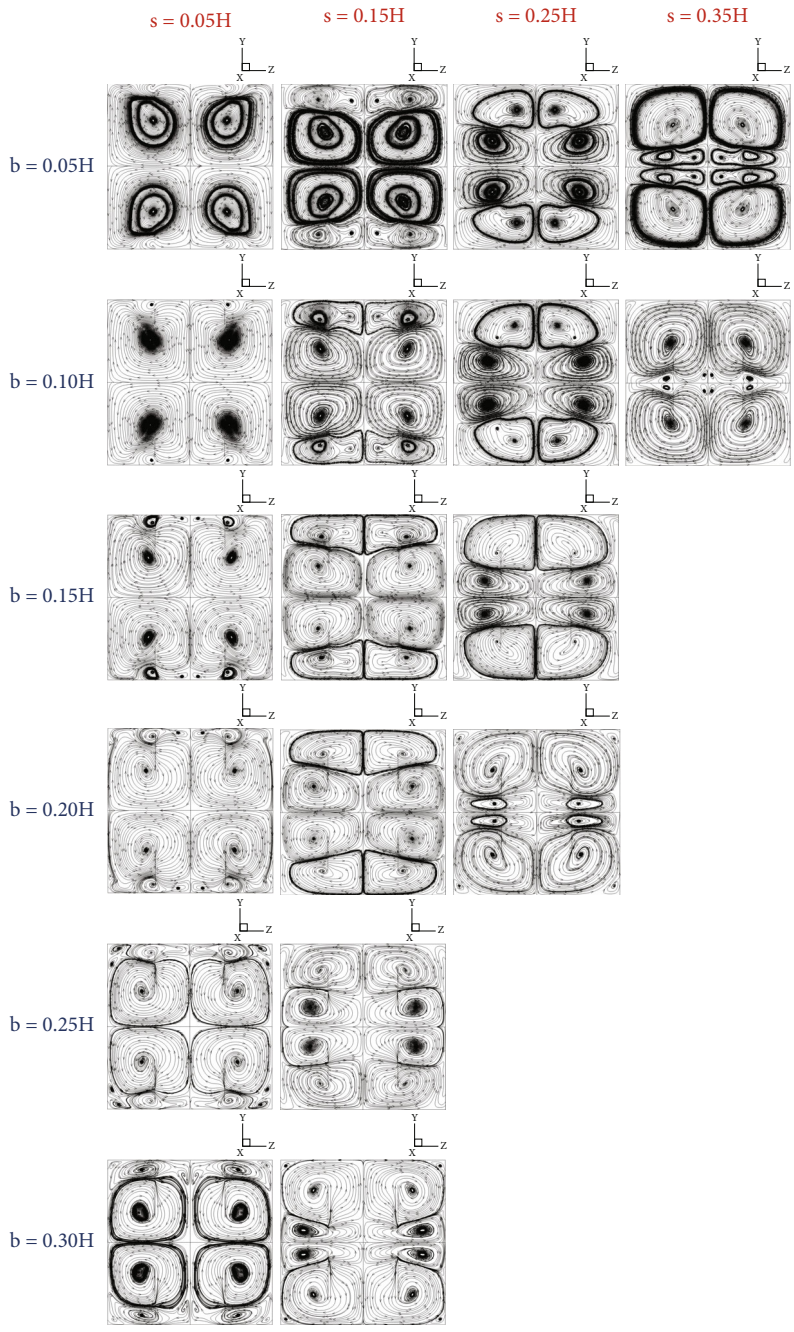

(a)

Figure 3: Continued.

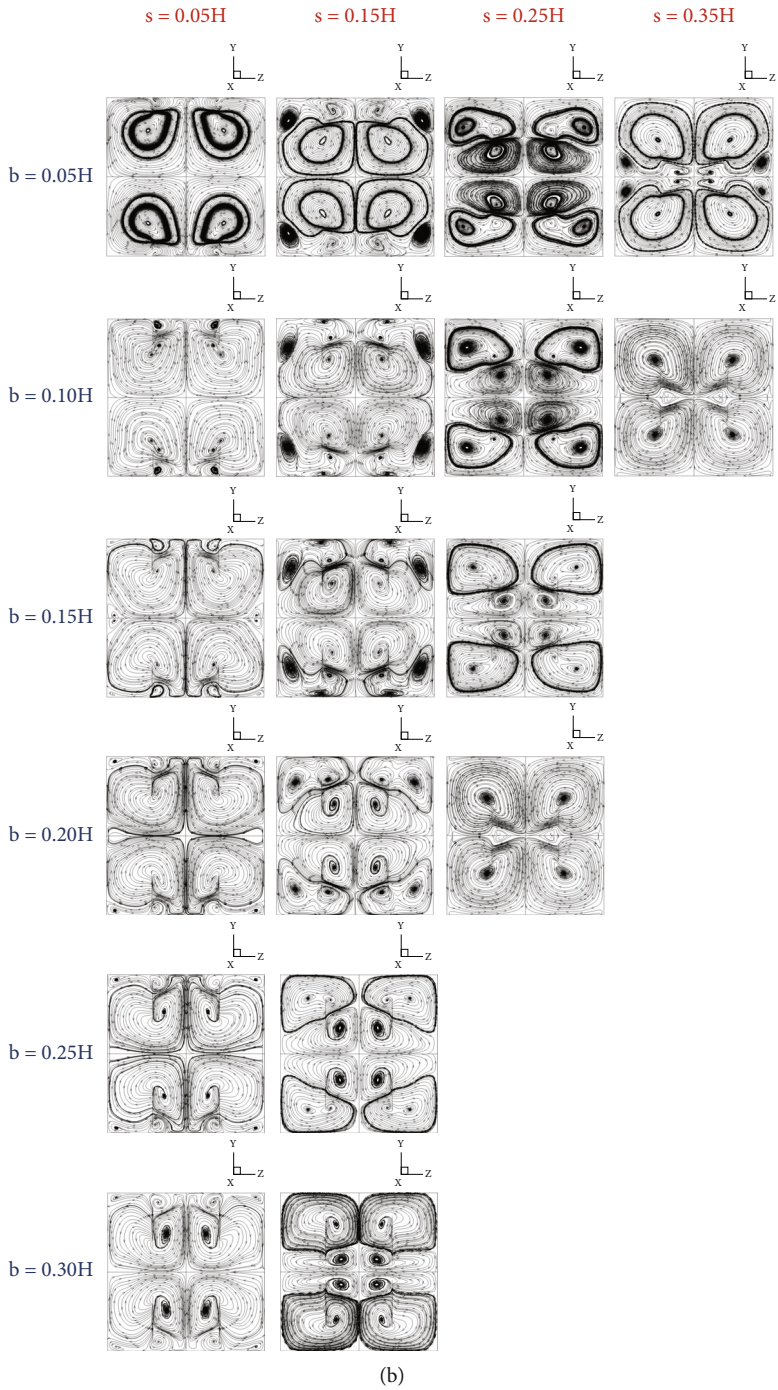

FIGURE 3: Streamlines in cross sectional planes for the baffled duct with various b/H and s/H at Re = 800 of (a) VD and (b) VU.

baffles, s, is also varied: 0.05H–0.40H, depending on the baffle height. The periodic length of the computational domain is represented with L, where $L/H = 1$. There are two flow directions: (1) V-Downstream (VD) or positive x ($+x$) and (2) V-Upstream (VU) or negative x ($-x$). The flow in the laminar regime with the Reynolds number between 100 and 2,000 (based on the entry condition) is considered for the present research.

A constant temperature at the duct walls of 310 K is set. The inlet and outlet zones of the baffled duct are applied with the periodic condition. The V-shaped baffle and V-shaped bar are applied as an insulator. The no-slip wall boundary is utilized for the whole surfaces of the baffled duct. Viscous dissipation is assumed to be negligible, and body force is not considered.

3. Mathematical Foundation

The assumptions for the numerical investigation are as follows.

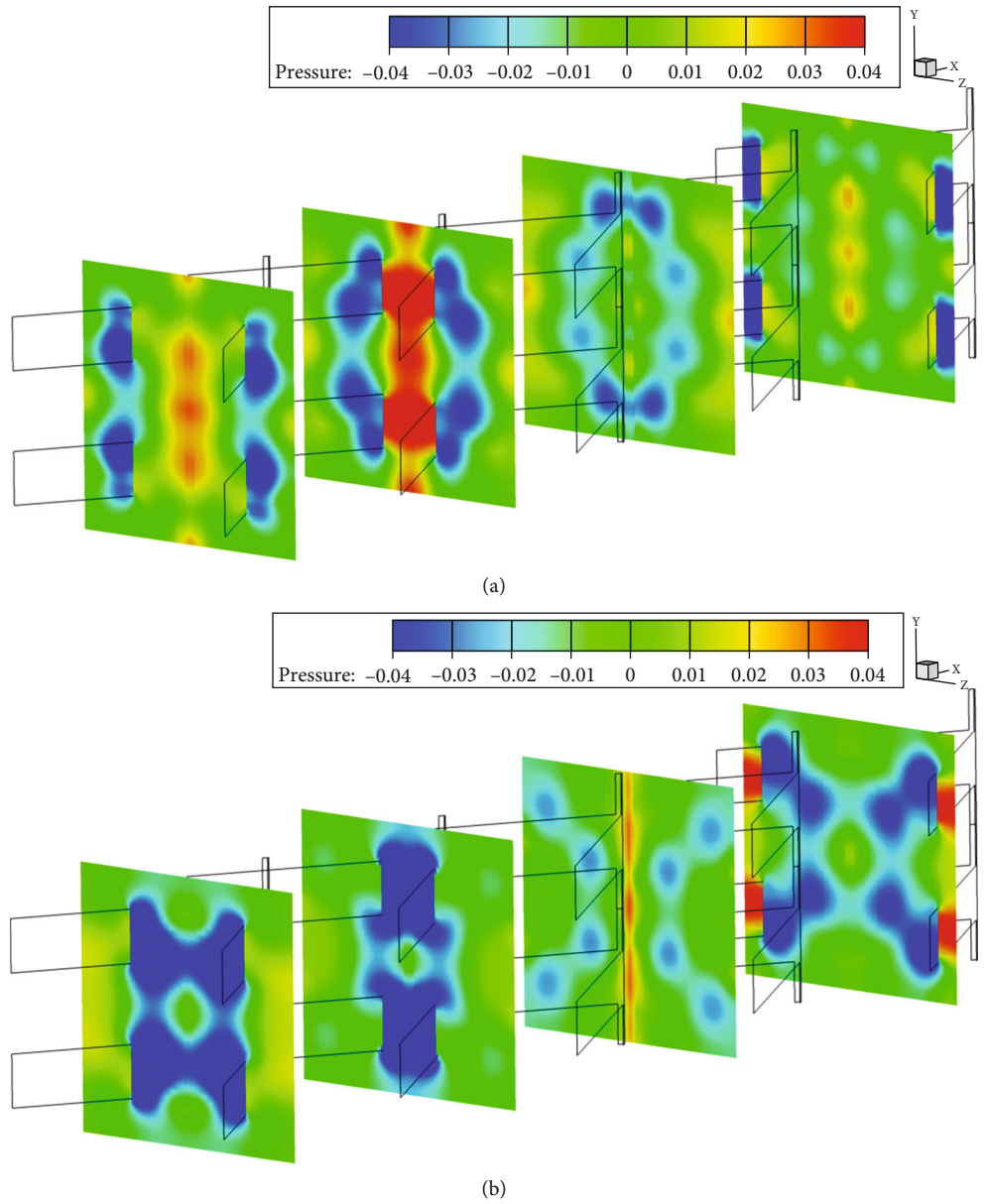

FIGURE 4: Pressure contours in transverse planes for the baffled duct with $b/H = 0.20$ and $s/H = 0.15$ at Re = 800 of (a) VD and (b) VU.

(i) Flow and heat transfer in the baffled duct are three-dimensional and steady-state problems

(ii) The tested fluid is air (considered as incompressible fluid because of its low velocity) at an initial temperature of 300 K with the Prandtl number of 0.707

(iii) The fluid properties are set to be constant because the variation of the fluid temperature is within ±10°C

(iv) Forced convective heat transfer is measured, while the radiation and the natural convection are not considered.

The continuity equation, the momentum equation, and the energy equation are expressed in Equations (1)–(3), respectively.

Continuity equation:

$$\frac{\partial}{\partial x_i}(\rho u_i) = 0. \tag{1}$$

Momentum equation:

$$\frac{\partial(\rho u_i u_j)}{\partial x_j} = -\frac{\partial p}{\partial x_i} + \frac{\partial}{\partial x_j}\left[\mu\left(\frac{\partial u_i}{\partial x_j} + \frac{\partial u_j}{\partial x_i}\right)\right]. \tag{2}$$

Energy equation:

$$\frac{\partial}{\partial x_i}(\rho u_i T) = \frac{\partial}{\partial x_j}\left(\Gamma \frac{\partial T}{\partial x_j}\right), \tag{3}$$

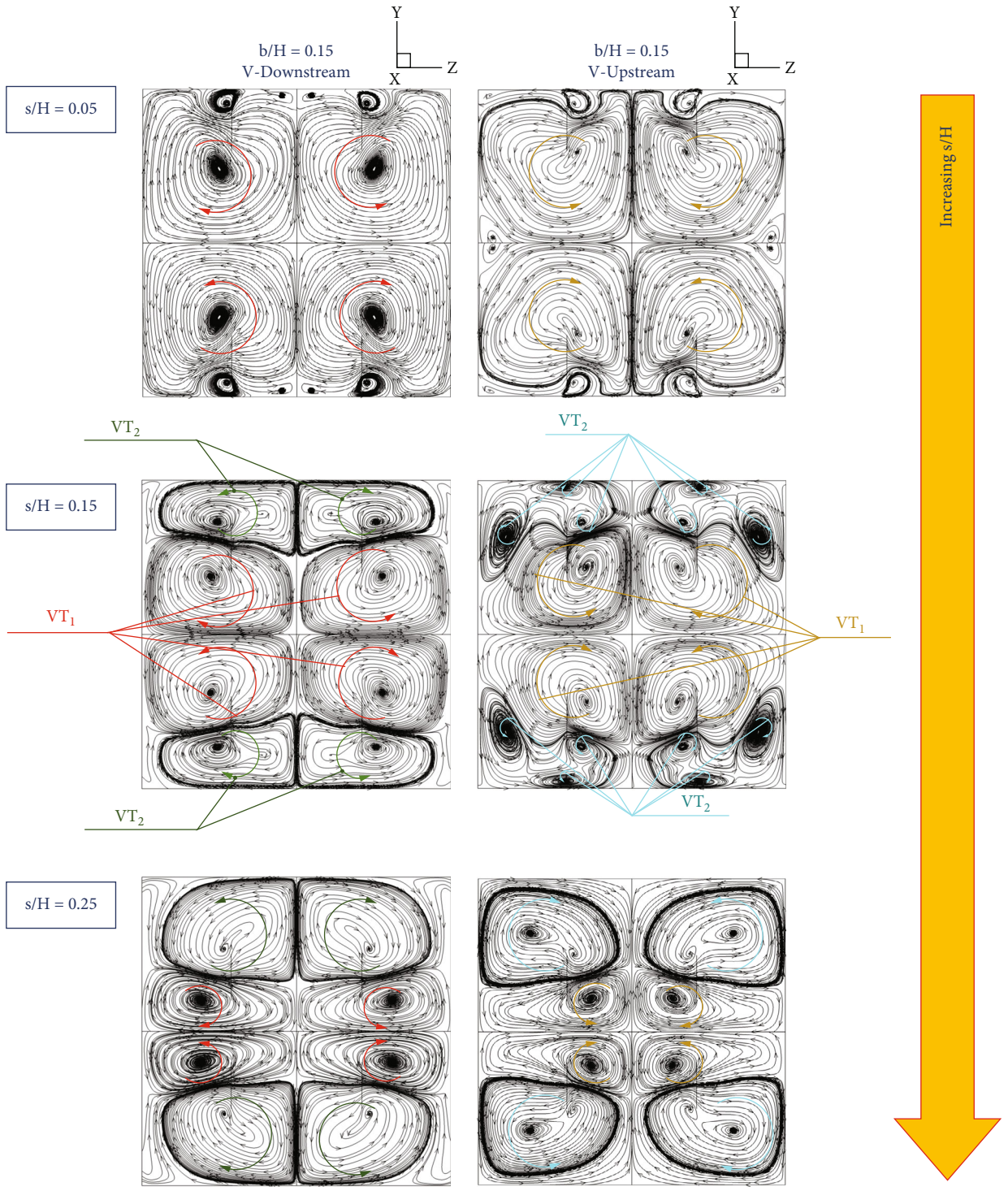

Figure 5: Flow structure at various s/H.

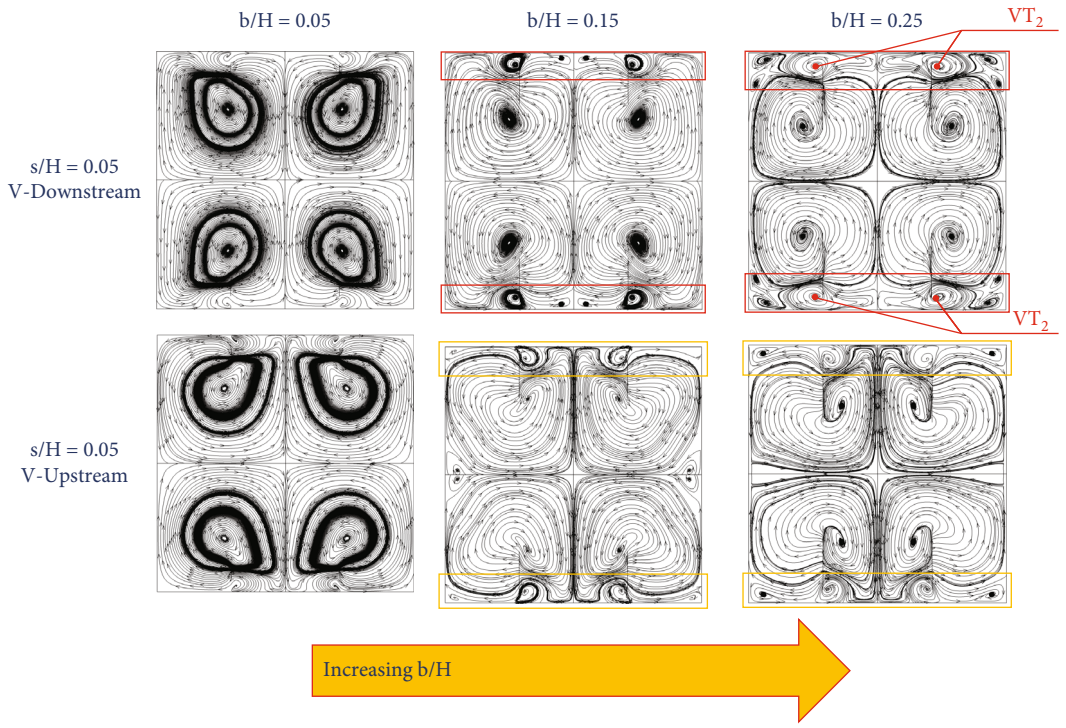

Figure 6: Flow structure at various b/H.

where Γ is the thermal diffusivity and is written as follows:

$$\Gamma = \frac{\mu}{\mathrm{Pr}}. \tag{4}$$

4. Numerical Method

The finite volume technique (a commercial code, ANSYS-FLUENT) is selected to solve the simulated problem of the baffled duct. The important equations of the present prediction are the continuity, the momentum, and the energy equations. For the simulated settings, the continuity and the momentum equations are discretized by the power law scheme, while the energy equation is discretized by the QUICK scheme. The simulated solutions are considered to be converged when the normalized residual data are lower than 10^{-5} for all variables but lower than 10^{-9} for the energy equation.

Five important variables of the present investigation are Reynolds number (Re), friction factor (f), local Nusselt number (Nu_x), average Nusselt number (Nu), and thermal enhancement factor (TEF).

The Reynolds number is written as

$$\mathrm{Re} = \frac{\rho \bar{u} D_h}{\mu}. \tag{5}$$

The pressure loss in the baffled duct is reported by the friction factor as

$$f = \frac{(\Delta p/L) D_h}{(1/2)\rho \bar{u}^2}. \tag{6}$$

The forced convective heat transfer in the baffled duct is assessed in terms of local Nusselt and averaged Nusselt number which can be determined by Equations (8) and (9), respectively.

$$q = k_f \left(\frac{\partial T}{\partial n}\right), \qquad h_x = \frac{q}{T_w - T_f}. \tag{7}$$

Subscript w is the wall, f is the local fluid, and n is the local coordinate normal to the wall.

$$Nu_x = \frac{h_x D_h}{k}, \tag{8}$$

$$Nu = \frac{1}{A}\int Nu_x \partial A. \tag{9}$$

The TEF is reported to describe the enhancement of the Nusselt number and friction factor in the baffled duct at similar pumping power. The TEF can be calculated as shown in

$$TEF = \left.\frac{h}{h_0}\right|_{pp} = \left.\frac{Nu}{Nu_0}\right|_{pp} = \left(\frac{Nu}{Nu_0}\right) \Big/ \left(\frac{f}{f_0}\right)^{1/3}. \tag{10}$$

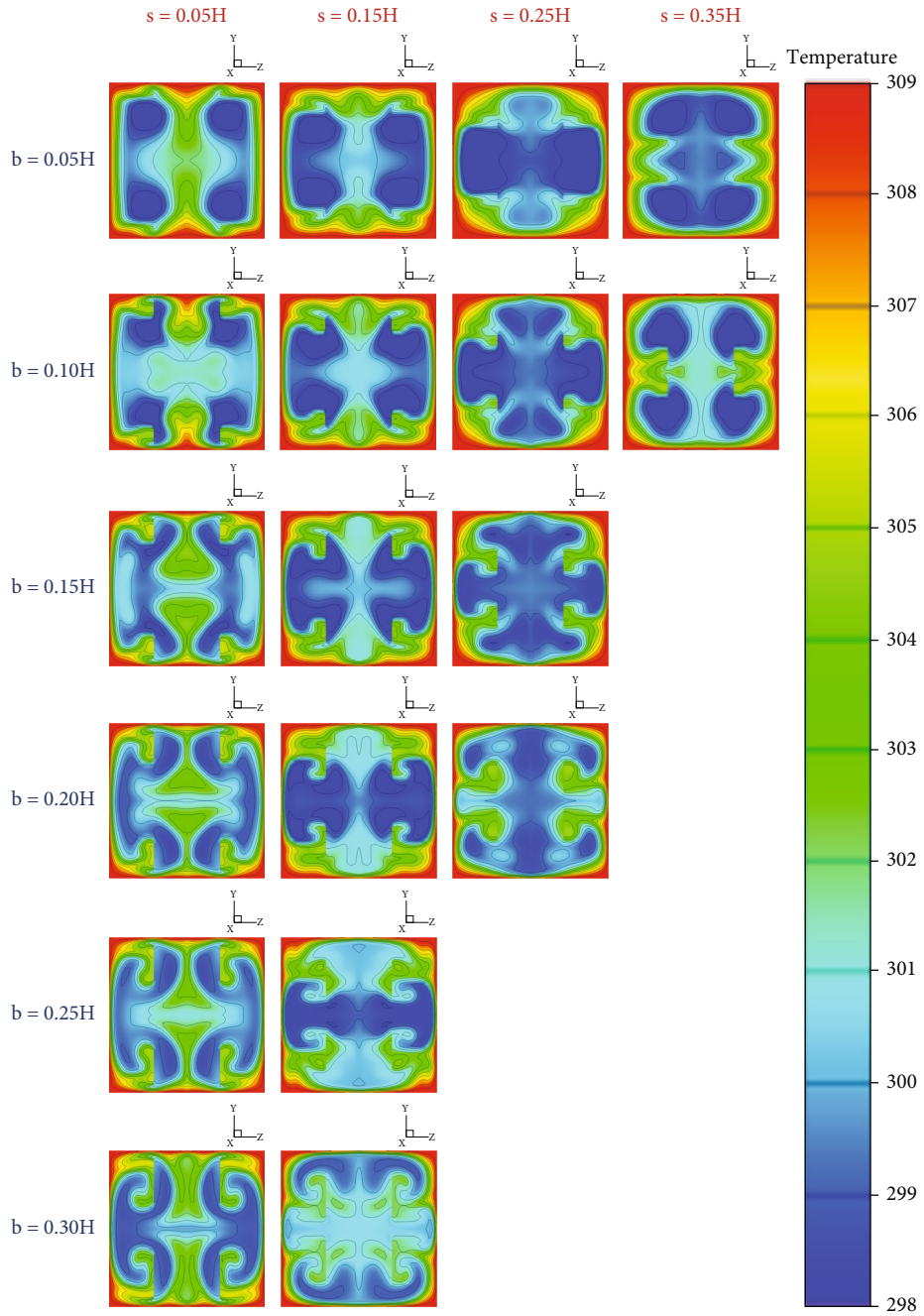

(a)

Figure 7: Continued.

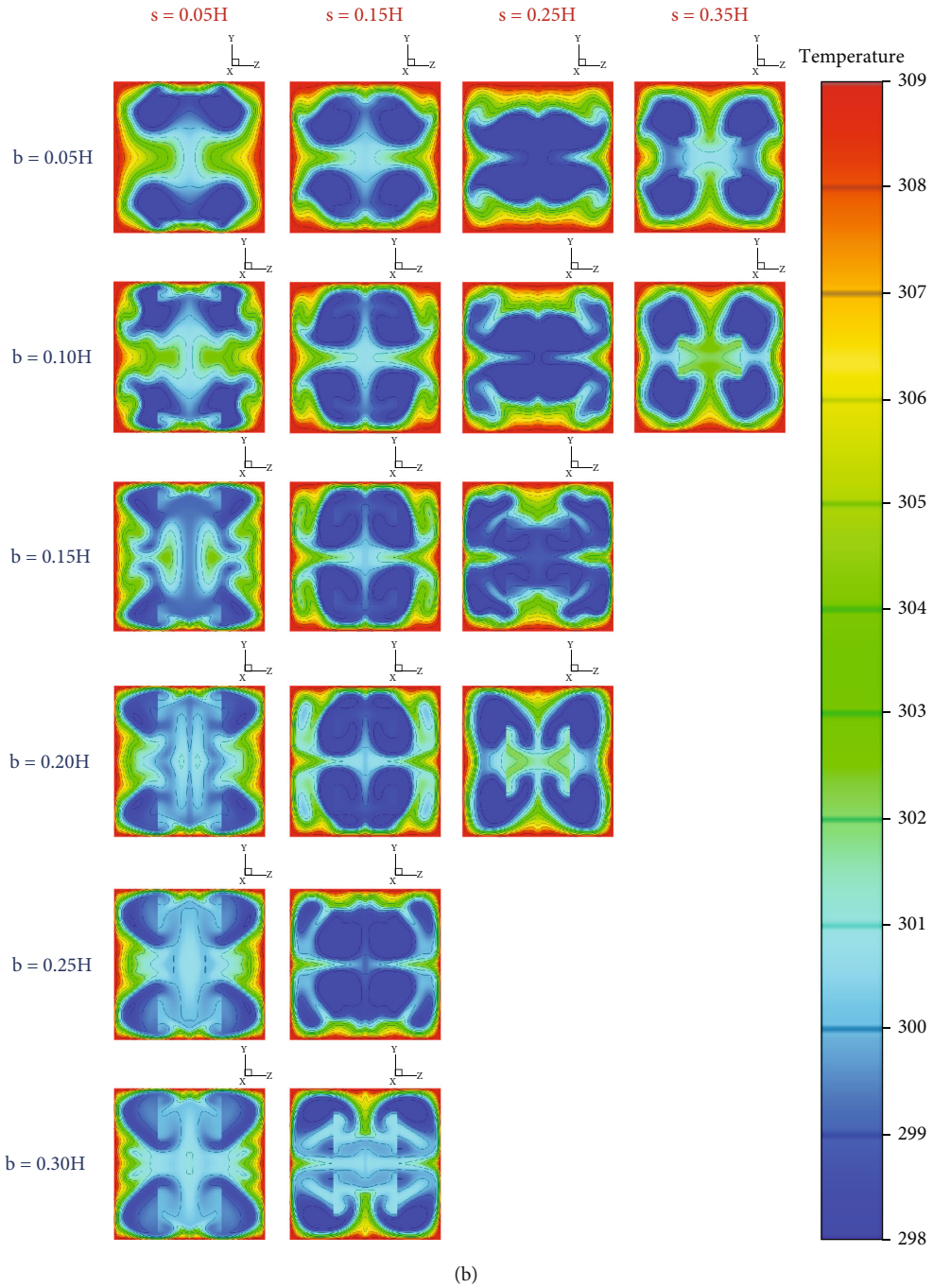

(b)

Figure 7: Temperature contours in cross-sectional planes for the baffled duct with various b/H and s/H at Re = 800 of (a) VD and (b) VU.

In Equation (10), Nu_0 is the Nusselt number and f_0 is the friction factor of the smooth duct with no baffle.

5. Numerical Results

5.1. Validation of Numerical Results. The validation of the numerical model of the baffled duct is divided into two parts: (1) smooth duct validation (Nusselt number and friction factor) and (2) grid independence. For the smooth duct validation, the Nusselt number and the friction factor of the present model are compared with the previously reported correlation [23]. The Nusselt number and the friction factor of the present research are in similar trends to the correlation data. The deviations of the Nusselt number and the friction factor are within ±2% as depicted in Figure 2.

For the grid independence, the simulated model (VD, $b/H = s/H = 0.15$) with different grid cells, 120000, 180000, 240000, and 360000, are compared. The Nusselt number and the friction factor of the present model and correlation data follow similar trends. The present values differ from

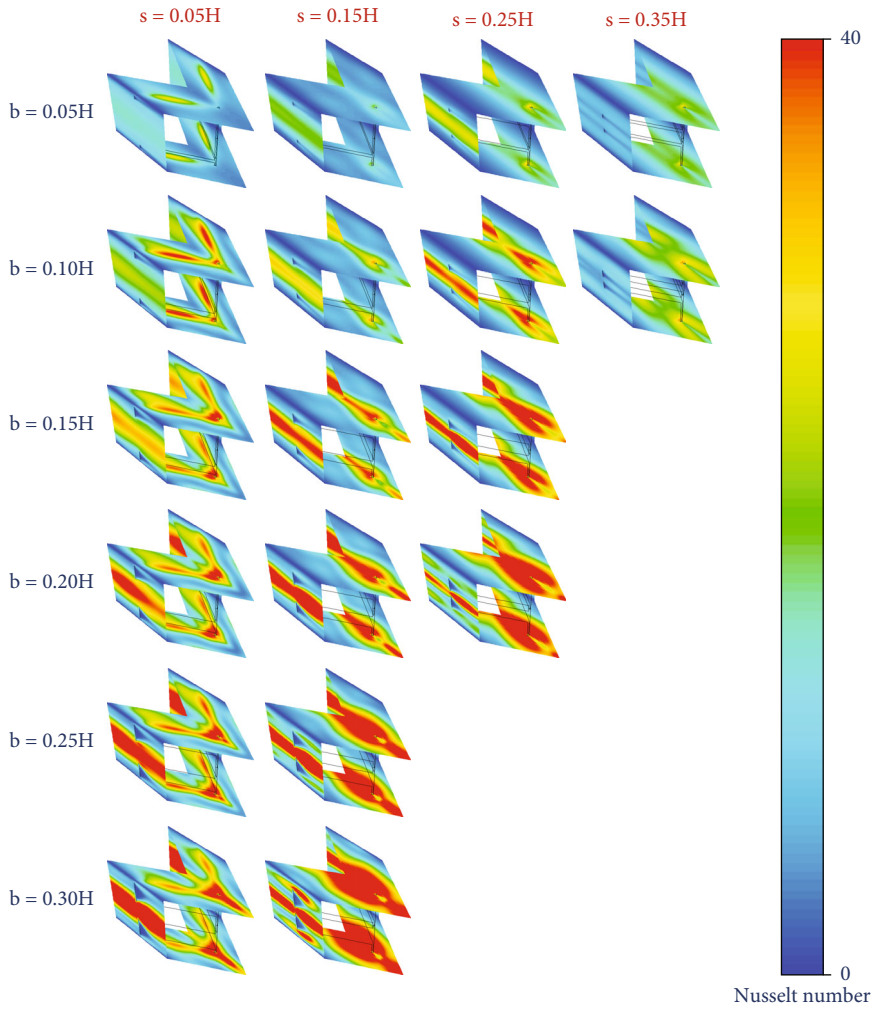

(a)

Figure 8: Continued.

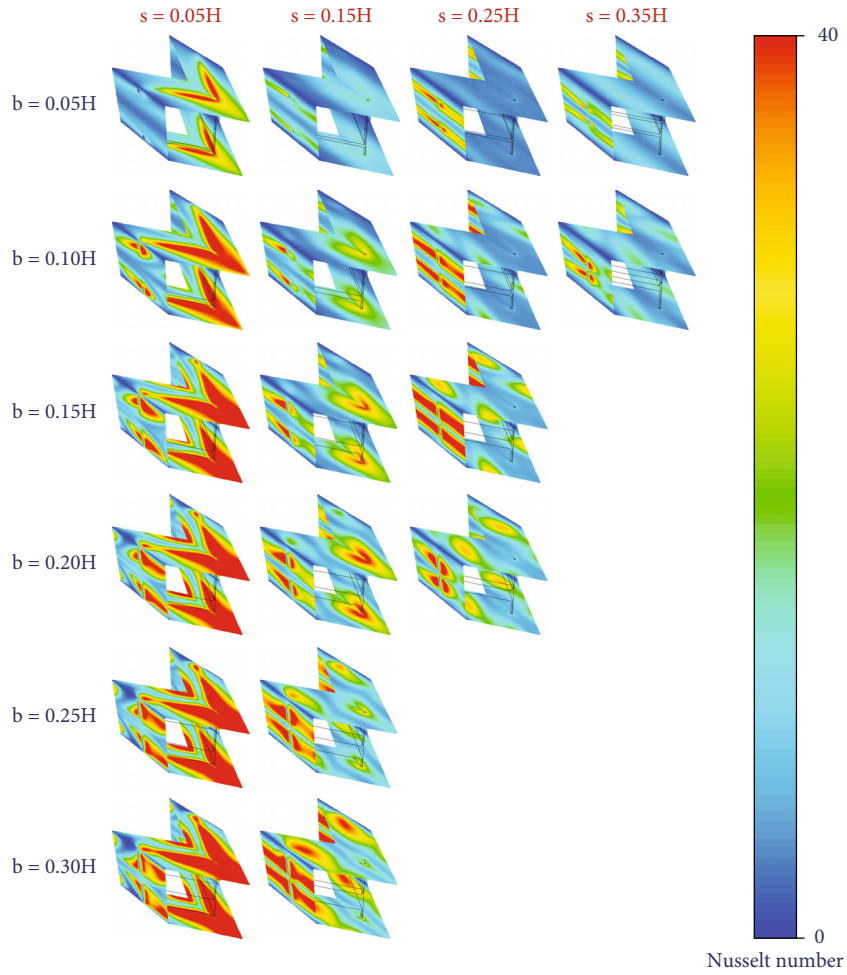

Figure 8: Local Nusselt number contours for the baffled duct with various b/H and s/H at Re = 800 of (a) VD and (b) VU.

the correlation values within ±2% when the augmented grid cell is higher than 180000. Thus, the simulated model is created with grid cells around 180000 for all investigated cases.

From this section, it can be concluded that the simulated model offers a reliable mean to study fluid flow and heat transfer profiles.

5.2. Fluid Flow and Heat Transfer Profiles. The streamlines in cross-sectional planes of the baffled duct with various s/H and b/H ratios are shown in Figures 3(a) and 3(b), respectively, for V-Downstream and V-Upstream directions. Generally, vortex flows are observed in all studied cases due to the pressure difference between in front of and behind the baffles (see Figure 4). The eight main vortex centers are observed. The flow structure changes when s/H, b/H, and flow directions are changed. There are two groups of the vortex flows: (1) Vortex no. 1 (VT_1) at the middle zone of the cross-sectional plane and (2) Vortex no. 2 (VT_2) at the upper-lower zones of the cross-sectional plane (see Figure 5). The VT_1 helps with fluid mixing, while the VT_2 disturbs the thermal boundary layer on heat transfer surfaces. When increasing s/H, the VT_2 extends, but the VT_1 contracts for both flow directions. When increasing b/H, the VT_2 slightly extends (see Figure 6).

Figures 7(a) and 7(b) show the temperature profiles in cross-sectional planes in the baffled duct with different b/H and s/H ratios for V-Downstream and V-Upstream, respectively. In general, better fluid mixing is observed in all cases. The disturbed thermal boundary layer is found near the tested duct walls. The temperature profile changes when the ratio of s/H and b/H and flow directions change. The disturbed thermal boundary layer is clearly detected when the b/H ratio increases. The disturbance of thermal boundary layer plays an important role in enhancing heat transfer coefficient.

Figures 8(a) and 8(b) show the local Nusselt number distributions on the baffled duct walls with various b/H and s/H ratios for V-Downstream and V-Upstream, respectively. The highest heat transfer coefficient is presented with the red contour, while the reversed result is plotted with the blue contour. The highest heat transfer coefficient is observed as a result of the disturbed thermal boundary layer caused by impinging flow. At similar s/H ratios, the local Nusselt number increases with an increase of baffle height. The $b = 0.30H$

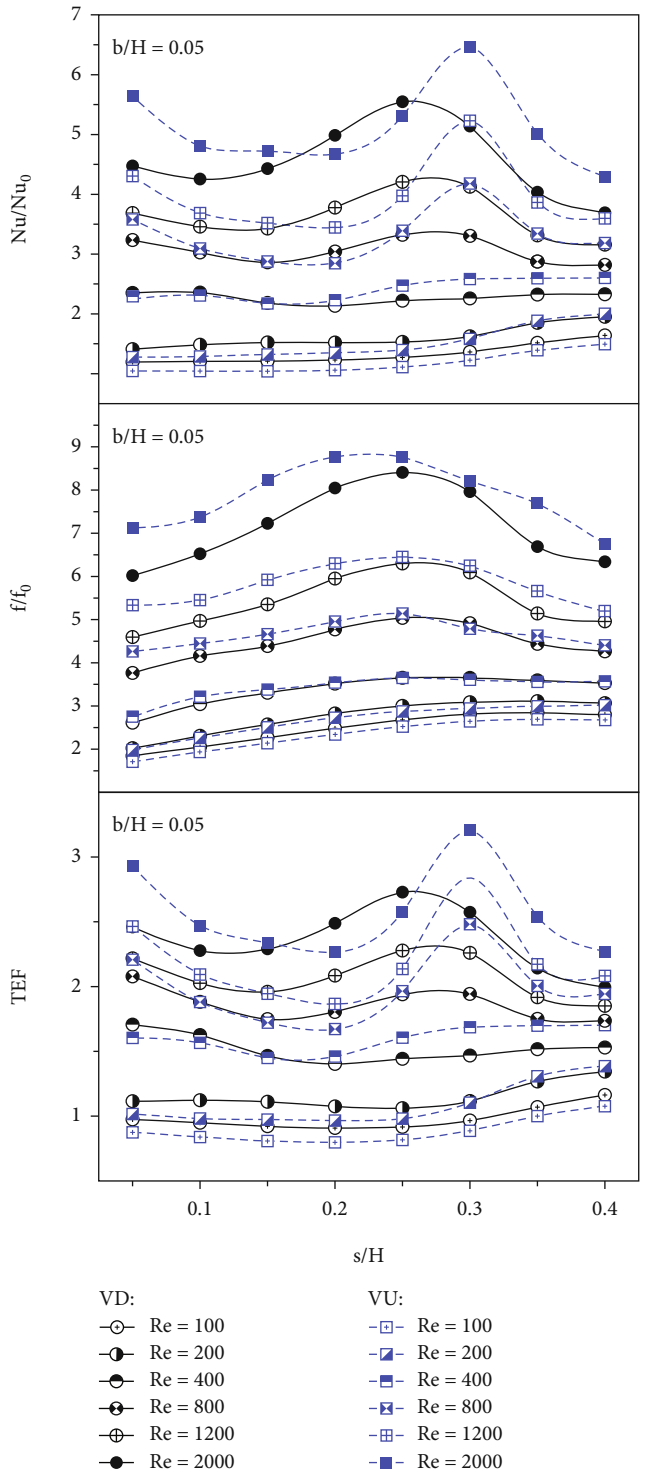

Figure 9: Thermal performance analysis of $b/H = 0.05$.

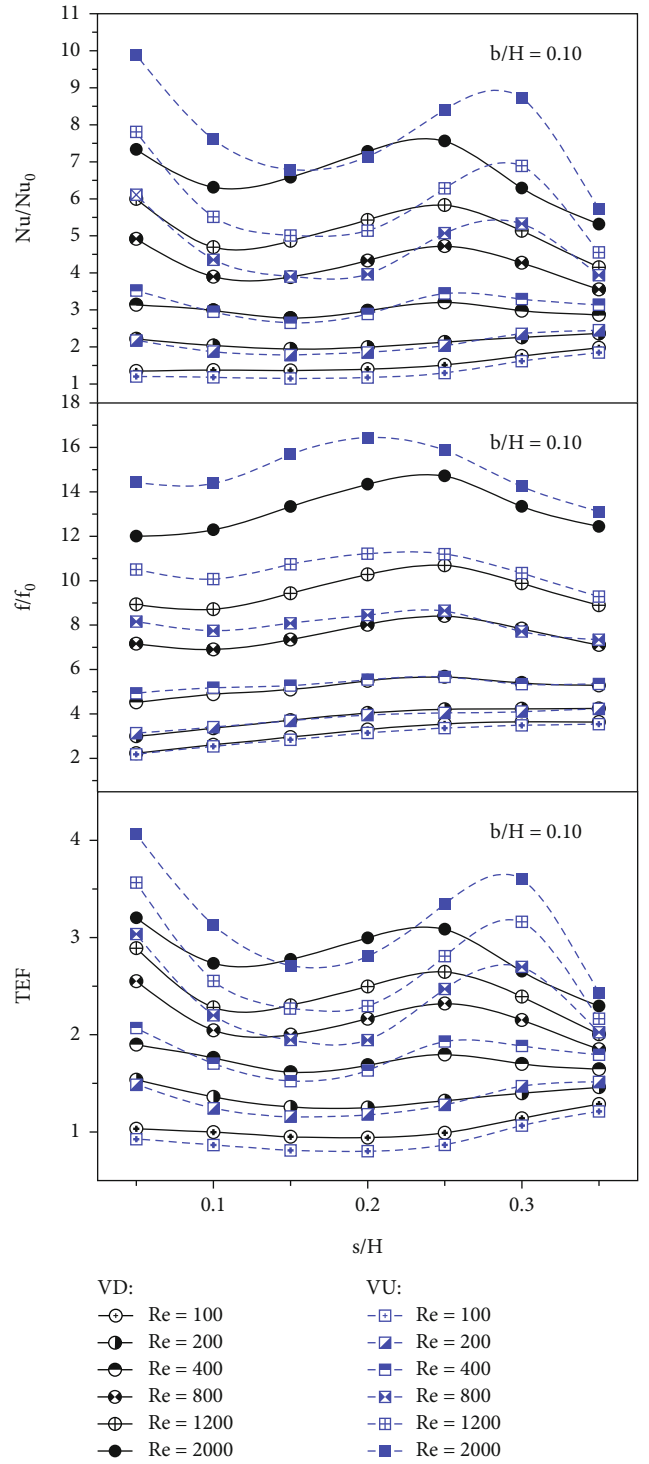

Figure 10: Thermal performance analysis of $b/H = 0.10$.

condition results in the highest heat transfer coefficient, while the $b = 0.05$H condition results in the lowest coefficient. The heat transfer profile does not follow similar patterns when changing the s/H ratio and the flow direction.

5.3. Thermal Performance Analysis. Figures 9–14 present the thermal performance analysis in terms of Nu/Nu_0, f/f_0, and TEF for the baffled duct with $b = 0.05$H, 0.10H, 0.15H, 0.20H, 0.25H, and 0.30H, respectively.

For the VD direction at Re = 2,000, the highest Nu/Nu_0 is observed at $s = 0.25$H, 0.25H, 0.20H, 0.20H, 0.15-0.20H, and 0.10H, and $b = 0.05$H, 0.10H, 0.15H, 0.20H, 0.25H, and 0.30H, respectively. For the VU direction at Re = 2,000 , the highest Nu/Nu_0 are obtained at $s = 0.05$H, except for

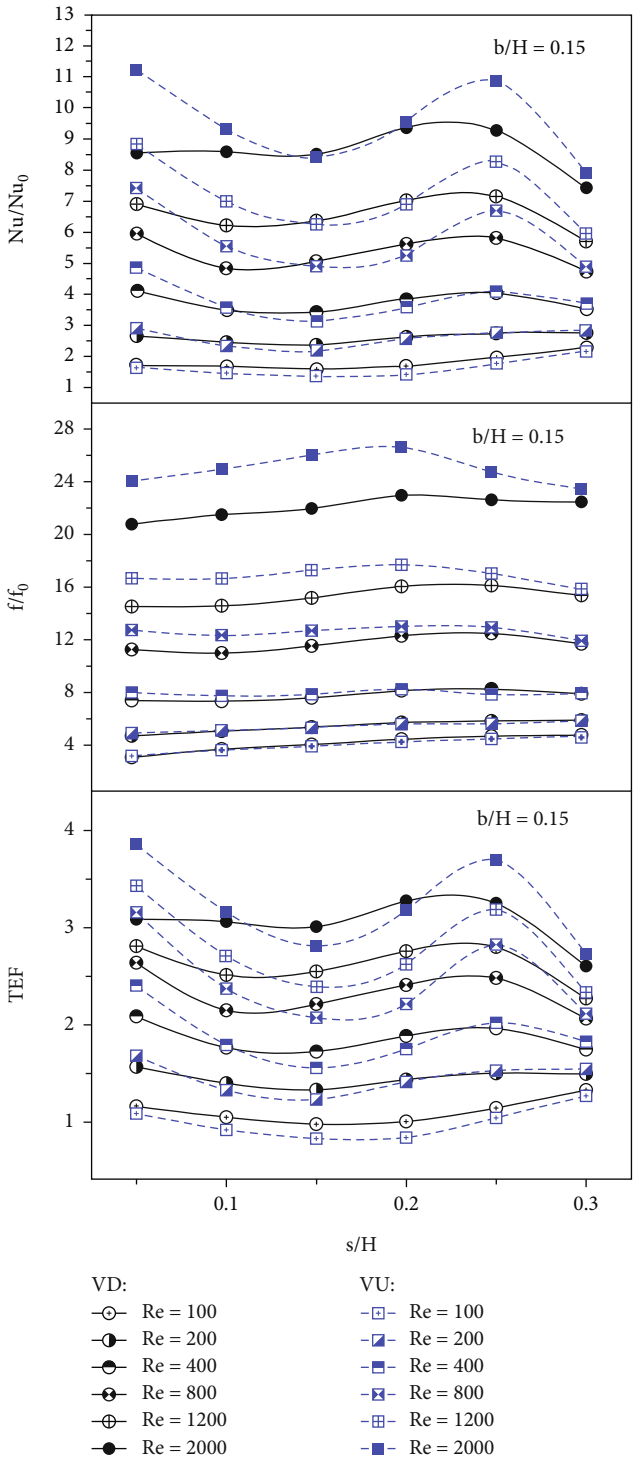

Figure 11: Thermal performance analysis of $b/H = 0.15$.

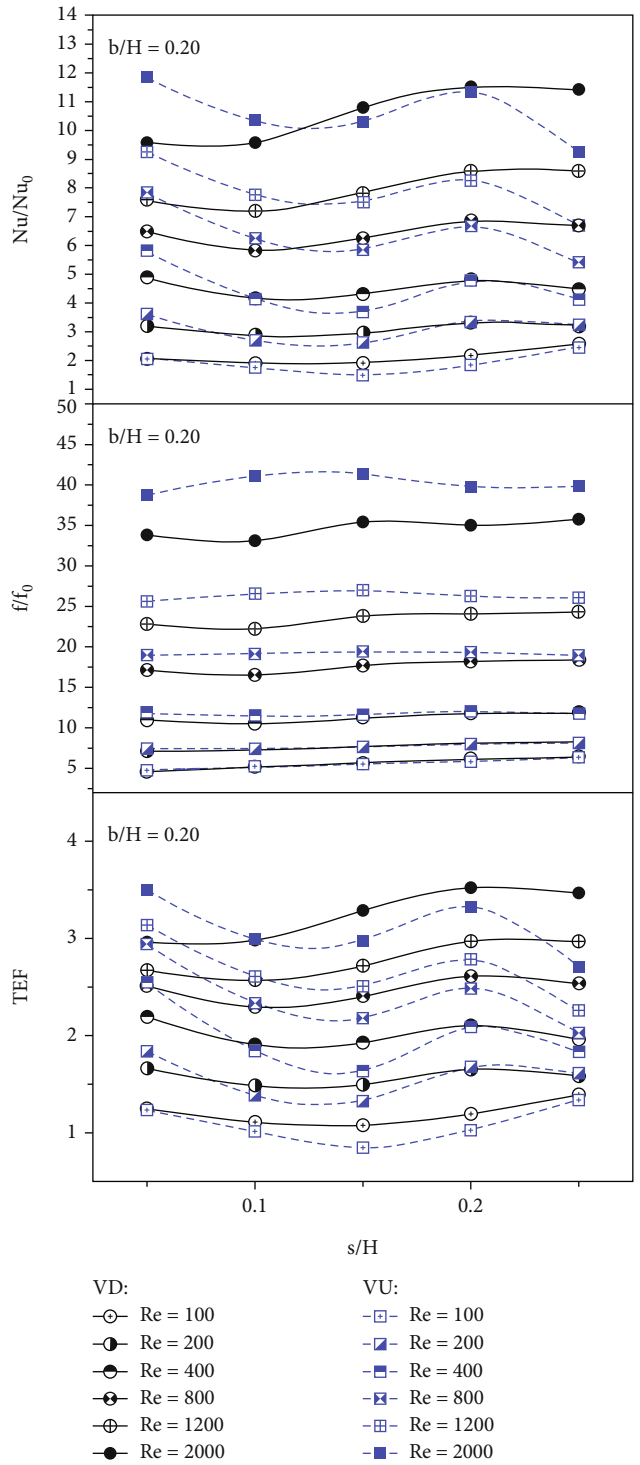

Figure 12: Thermal performance analysis of $b/H = 0.20$.

$b = 0.05$H which the highest Nu/Nu_0 is observed at $s = 0.30$ H. The Nusselt number of the baffled duct is found to be 1.19–15.55 and 1.04–15.07 times greater than the smooth duct for both VD and VU directions, respectively.

For the VD direction at Re = 2,000, the maximum f/f_0 is found at $s = 0.25$H, 0.25H, 0.20H, 0.25H, 0.20H, and 0.15H when $b = 0.05$H, 0.10H, 0.15H, 0.20H, 0.25H, and 0.30H, respectively. For the VU direction at Re =2,000, the highest f/f_0 is found at $s = 0.20 - 0.25$H, 0.20H, 0.20H, 0.15H, 0.10H, and 0.05–0.10H when $b = 0.05$H, 0.10H, 0.15H, 0.20H, 0.25H, and 0.30H, respectively. In the studied condition, the friction factor of the baffled duct for the VD and VU directions is 1.84–98.46 and 1.71–112.08 times, respectively, greater than that of the plain duct.

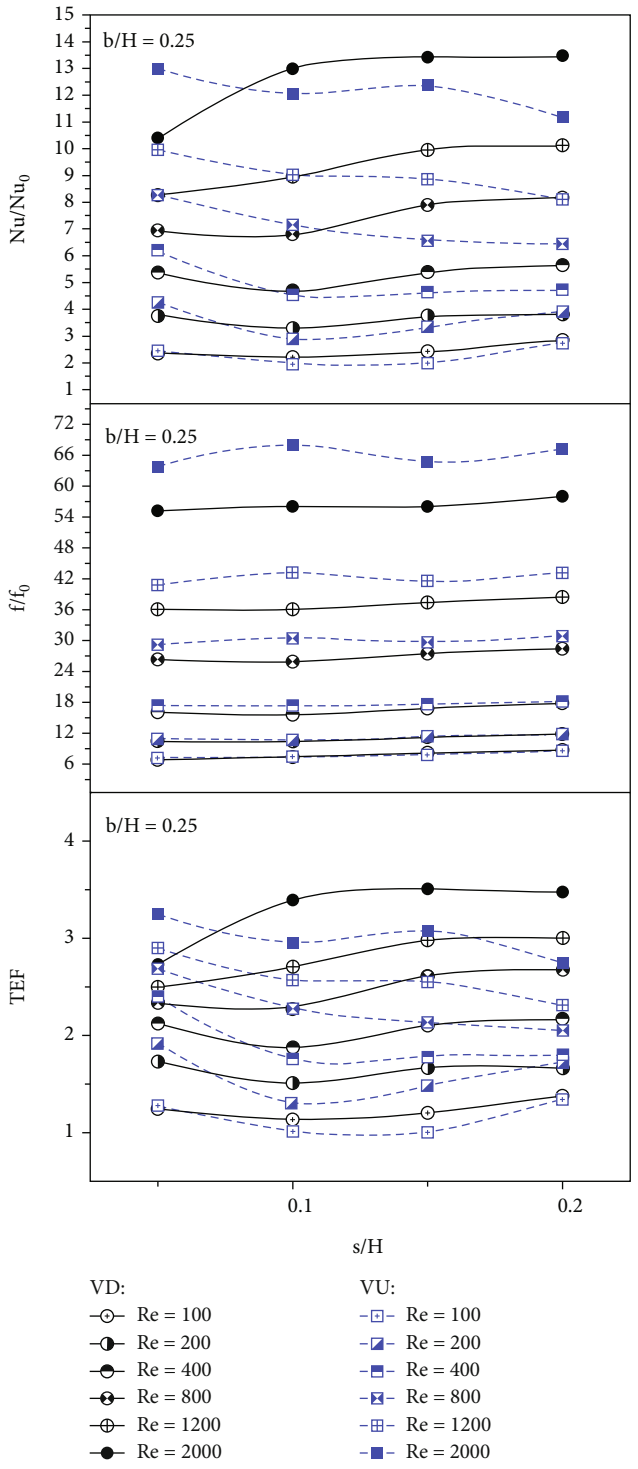

Figure 13: Thermal performance analysis of b/H =0.25.

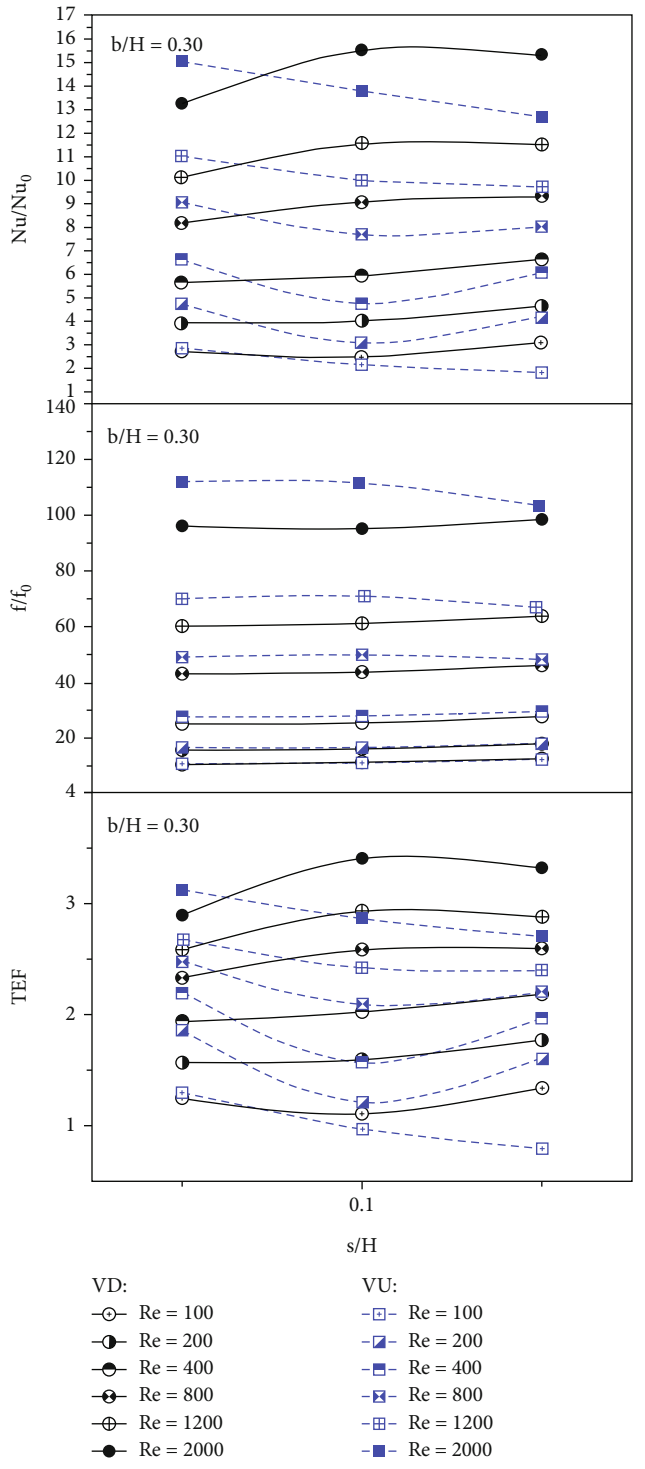

Figure 14: Thermal performance analysis of $b/H = 0.30$.

For the VD direction at Re = 2,000, the highest TEF of the baffled duct is observed at $s = 0.25$H, 0.05H, 0.20H, 0.20H, 0.15H, and 0.10H when $b = 0.05$H, 0.10H, 0.15H, 0.20H, 0.25H, and 0.30H, respectively.

For the VU direction at Re = 2,000, the optimal TEF of is observed at $s = 0.05$H, except for $b = 0.05$H which the highest TEF is observed at $s = 0.30$H. In addition, the maximum TEF of 4.06 is found at Re = 2,000, $b/H = 0.10$, and $s/H = 0.05$ for the VU direction (see Figure 15).

The comparison between the numerical results from this present study and those from previous works [24–27] is shown in Figure 16. Figure 16(a) shows that the present

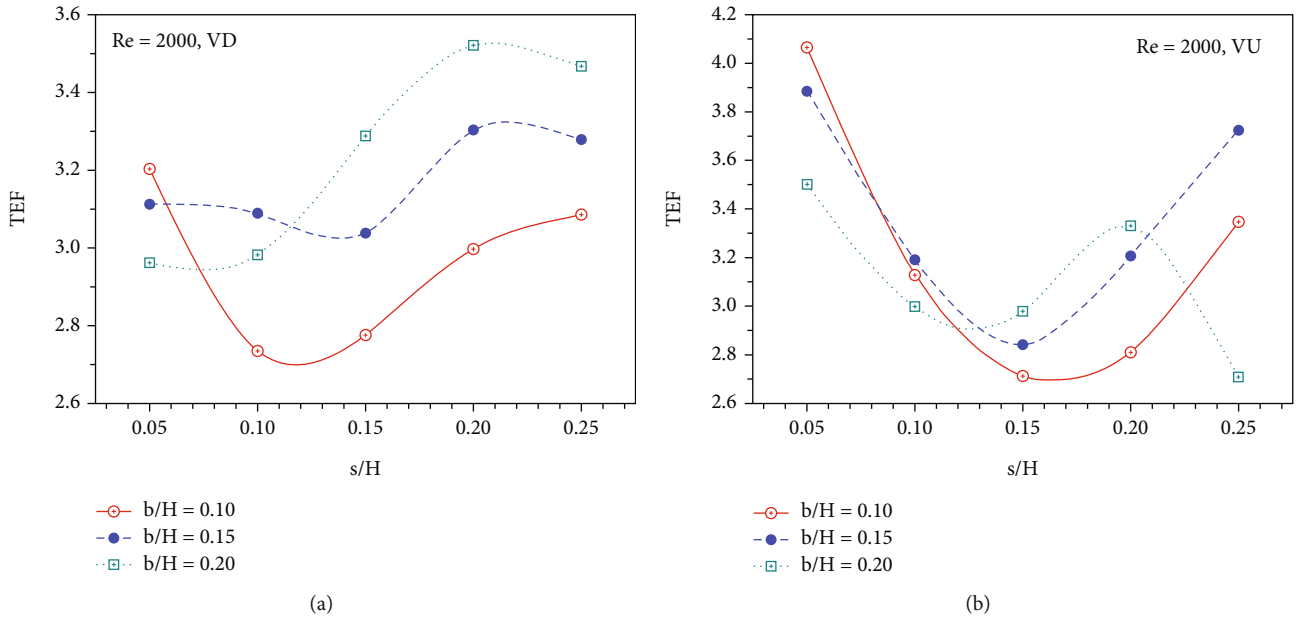

Figure 15: TEF vs. s/H for $b = 0.10H - 0.20H$ of (a) VD and (b) VU.

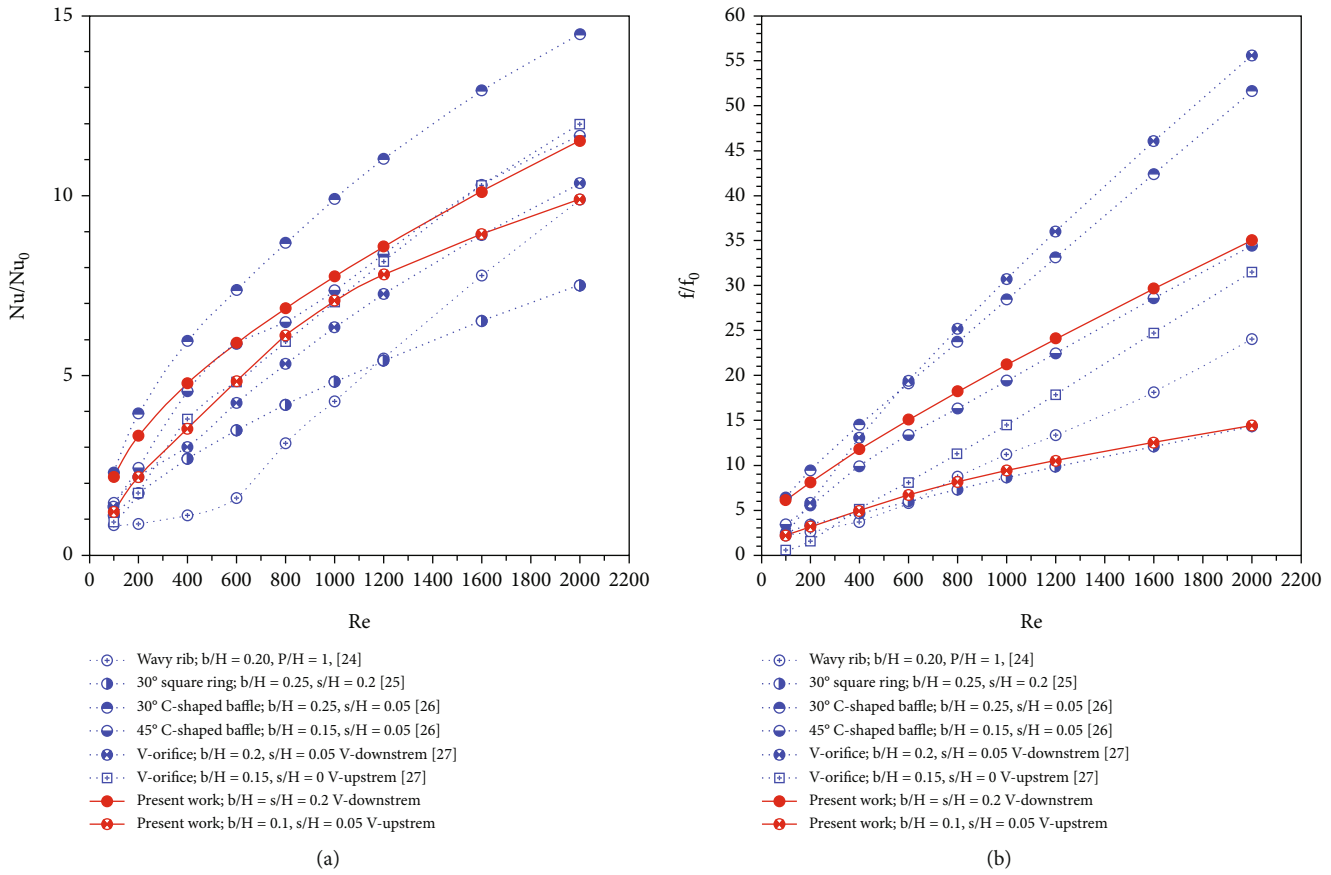

Figure 16: Continued.

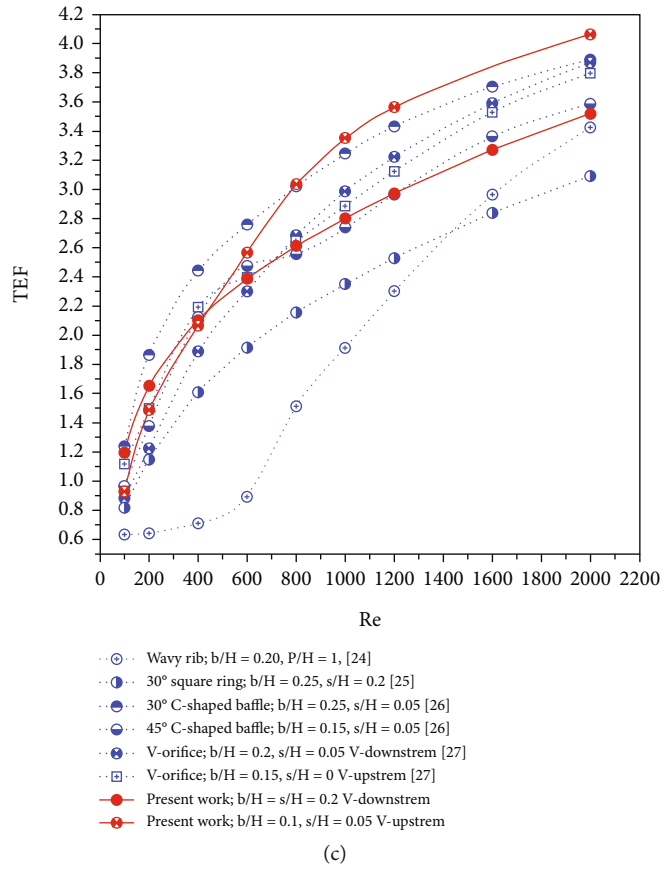

(c)

Figure 16: Comparison with the previous works for (a) Nu/Nu_0, (b) f/f_0, and (c) TEF.

vortex generator provides lower heat transfer rate than the V-orifice [27]. However, as shown in Figure 16(b), there is lower friction loss generated by the present vortex generator compared with the V-orifice [27]. Therefore, from Figure 16(c), TEF of the present generator offers the best thermal performance.

6. Conclusion

Numerical analysis on fluid flows and heat transfer profiles in the baffled duct is presented. The effects of baffle height ($b/H = 0.05 - 0.30$), baffle location ($s/H = 0.05 - 0.40$), and flow directions (VD and VU) are examined in the laminar flow regime ($Re = 100 - 2{,}000$). The main findings can be concluded as follows.

The important mechanisms such as impinging flow, vortex flow, and disturbed thermal boundary layer which help to improve the heat transfer coefficient are observed in the baffled duct. The flow and heat transfer profiles in the baffled duct change when varying the ratios of s/H and b/H and flow directions. The baffle location is a significant factor for the variations of the flow and heat transfer mechanisms in the baffled duct.

In the investigated range, the heat transfer rate and the friction loss of the baffled duct are 1.04–15.55 and 1.71–112.08 times, respectively, higher than the smooth duct with no baffle. The TEF of the baffled duct ranges from 1.00 to 4.06, depending on the ratios of b/H and s/H, Re, and flow directions.

The present baffle configuration has more stability than the general V-shaped baffle with no V-bar and easy to install and maintenance in heat exchanger systems. The present baffle remains TEF and heat transfer coefficient close to the general type of the V-shaped baffle.

Nomenclature

b: Baffle height, m
D_h: Hydraulic diameter of the duct, m
f: Friction factor
H: Square duct height, m
h: Convective heat transfer coefficient, W m^{-2} K^{-1}
k: Thermal conductivity, W m^{-1} K^{-1}
L: Numerical model length, m
Nu: Nusselt number ($=hD_h/k$)
p: Static pressure, Pa
Re: Reynolds number
s: Gap spacing between upper/lower duct walls and upper/lower baffle edges, m
T: Temperature, K

$\bar{u}$: Mean velocity in channel, m s^{-1}
W: Duct width, m.

Greek Letters

α: Flow attack angle, degree
TEF: Thermal enhancement factor
ρ: Density, kg m^{-3}.

Subscript

0: Smooth square channel
pp: Pumping power

Data Availability

No data were used to support this study.

Conflicts of Interest

The authors declare that there is no conflict of interest regarding the publication of this article.

Acknowledgments

The authors would like to acknowledge Assoc. Prof. Dr. Pongjet Promvonge for suggestions. This work is supported by King Mongkut's Institute of Technology Ladkrabang (2565-02-01-088).

References

[1] A. Boonloi and W. Jedsadaratanachai, "Thermal performance analysis and empirical correlations for laminar forced convection over 30° V-baffled square channel," *Advances in Mechanical Engineering*, vol. 6, Article ID 930272, 2014.

[2] P. Zhang, Y. Rao, Y. Xie, and M. Zhang, "Turbulent flow structure and heat transfer mechanisms over surface vortex structures of micro V-shaped ribs and dimples," *International Journal of Heat and Mass Transfer*, vol. 178, article 121611, 2021.

[3] H. Xiao, Z. Liu, and W. Liu, "Turbulent heat transfer enhancement in the mini-channel by enhancing the original flow pattern with v-ribs," *International Journal of Heat and Mass Transfer*, vol. 163, article 120378, 2020.

[4] M. Bahiraei, N. Mazaheri, and H. Moayedi, "Employing V-shaped ribs and nanofluid as two passive methods to improve second law characteristics of flow within a square channel: a two-phase approach," *International Journal of Heat and Mass Transfer*, vol. 151, article 119419, 2020.

[5] P. K. Jain and A. Lanjewar, "Overview of V-RIB geometries in solar air heater and performance evaluation of a new V-RIB geometry," *Renewable Energy*, vol. 133, pp. 77–90, 2019.

[6] D. Jin, S. Quan, J. Zuo, and S. Xu, "Numerical investigation of heat transfer enhancement in a solar air heater roughened by multiple V-shaped ribs," *Renewable Energy*, vol. 134, pp. 78–88, 2019.

[7] M. Bahiraei, N. Mazaheri, Y. Hosseini, and H. Moayedi, "A two-phase simulation for analyzing thermohydraulic performance of Cu-water nanofluid within a square channel enhanced with 90° V-shaped ribs," *International Journal of Heat and Mass Transfer*, vol. 145, article 118612, 2019.

[8] R. Misra, J. Singh, S. K. Jain et al., "Prediction of behavior of triangular solar air heater duct using V-down rib with multiple gaps and turbulence promoters as artificial roughness: a CFD analysis," *International Journal of Heat and Mass Transfer*, vol. 162, article 120376, 2020.

[9] D. Jin, J. Zuo, S. Quan, S. Xu, and H. Gao, "Thermohydraulic performance of solar air heater with staggered multiple V-shaped ribs on the absorber plate," *Energy*, vol. 127, pp. 68–77, 2017.

[10] D. Jin, M. Zhang, P. Wang, and S. Xu, "Numerical investigation of heat transfer and fluid flow in a solar air heater duct with multi V-shaped ribs on the absorber plate," *Energy*, vol. 89, pp. 178–190, 2015.

[11] A. Kumar and M. H. Kim, "Heat transfer and fluid flow characteristics in air duct with various V-pattern rib roughness on the heated plate: a comparative study," *Energy*, vol. 103, pp. 75–85, 2016.

[12] S. Singh, S. Chander, and J. S. Saini, "Investigations on thermohydraulic performance due to flow-attack-angle in V-down rib with gap in a rectangular duct of solar air heater," *Applied Energy*, vol. 97, pp. 907–912, 2012.

[13] N. S. Deo, S. Chander, and J. S. Saini, "Performance analysis of solar air heater duct roughened with multigap V-down ribs combined with staggered ribs," *Renewable Energy*, vol. 91, pp. 484–500, 2016.

[14] R. K. Ravi and R. P. Saini, "Nusselt number and friction factor correlations for forced convective type counter flow solar air heater having discrete multi V shaped and staggered rib roughness on both sides of the absorber plate," *Applied Thermal Engineering*, vol. 129, pp. 735–746, 2018.

[15] S. Caliskan and S. Baskaya, "Experimental investigation of impinging jet array heat transfer from a surface with V-shaped and convergent-divergent ribs," *International Journal of Thermal Sciences*, vol. 59, pp. 234–246, 2012.

[16] S. Singh, S. Chander, and J. S. Saini, "Exergy based analysis of solar air heater having discrete V-down rib roughness on absorber plate," *Energy*, vol. 37, no. 1, pp. 749–758, 2012.

[17] R. Karwa and G. Chitoshiya, "Performance study of solar air heater having v-down discrete ribs on absorber plate," *Energy*, vol. 55, pp. 939–955, 2013.

[18] P. Singh and S. Ekkad, "Experimental study of heat transfer augmentation in a two-pass channel featuring V-shaped ribs and cylindrical dimples," *Applied Thermal Engineering*, vol. 116, pp. 205–216, 2017.

[19] A. Kumar, R. P. Saini, and J. S. Saini, "Development of correlations for Nusselt number and friction factor for solar air heater with roughened duct having multi V-shaped with gap rib as artificial roughness," *Renewable Energy*, vol. 58, pp. 151–163, 2013.

[20] R. K. Ravi and R. P. Saini, "Experimental investigation on performance of a double pass artificial roughened solar air heater duct having roughness elements of the combination of discrete multi V shaped and staggered ribs," *Energy*, vol. 116, pp. 507–516, 2016.

[21] M. P. Boruah, P. R. Randive, and S. Pati, "Hydrothermal performance and entropy generation analysis for mixed convective flows over a backward facing step channel with baffle," *International Journal of Heat and Mass Transfer*, vol. 125, pp. 525–542, 2018.

[22] M. P. Boruah, S. Pati, and P. R. Randive, "Implication of fluid rheology on the hydrothermal and entropy generation

characteristics for mixed convective flow in a backward facing step channel with baffle," *International Journal of Heat and Mass Transfer*, vol. 137, pp. 138–160, 2019.

[23] Y. A. Cengel and A. J. Ghajar, *Heat and Mass Transfer: Fundamentals & Applications, Fifth edition in SI Units*, McGraw-Hill Education, 2015, ISBN 978-981-4595-27-8.

[24] A. Boonloi and W. Jedsadaratanachai, "Forced convective heat transfer and thermal efficiency assessment in square channel equipped with 10° wavy thin rib," *Advances in Mechanical Engineering*, vol. 12, no. 12, Article ID 168781402098526, 2020.

[25] A. Boonloi and W. Jedsadaratanachai, "Influence of ring size and location on flow topology, heat transfer structure and thermal efficiency in heat exchanger square channel placed with 30-degree inclined square ring," *Frontiers in Heat and Mass Transfer*, vol. 13, 2020.

[26] A. Boonloi and W. Jedsadaratanachai, "Flow and heat transfer characteristics of air in square channel heat exchanger with C-shaped baffle: a numerical study," *Frontiers in Heat and Mass Transfer*, vol. 13, 2019.

[27] A. Boonloi and W. Jedsadaratanachai, "The effects of gap spacing ratio on flow structure and heat transfer characteristic for the V-orifice in the square channel heat exchanger," *Frontiers in Heat and Mass Transfer*, vol. 12, 2019.